

# Lipid imaging by gold cluster time-of-flight secondary ion mass spectrometry: application to Duchenne muscular dystrophy

David Touboul,\* Alain Brunelle,<sup>1,\*</sup> Frédéric Halgand,\* Sabine De La Porte,<sup>†</sup> and Olivier Laprèvote\*

Laboratoire de Spectrométrie de Masse,\* Institut de Chimie des Substances Naturelles, Centre National de la Recherche Scientifique, Unité Propre de Recherche 2301, F91198 Gif sur Yvette Cedex, France; and Laboratoire de Neurobiologie Cellulaire et Moléculaire,<sup>†</sup> Institut de Neurobiologie Alfred Fessard, Centre National de la Recherche Scientifique, Unité Propre de Recherche 9040, F91198 Gif sur Yvette Cedex, France

**Abstract** Imaging with time-of-flight secondary ion mass spectrometry (TOF-SIMS) has expanded very rapidly with the development of gold cluster ion sources ( $\text{Au}_3^+$ ). It is now possible to acquire ion density maps (ion images) on a tissue section without any treatment and with a lateral resolution of few micrometers. In this article, we have taken advantage of this technique to study the degeneration/regeneration process in muscles of a Duchenne muscular dystrophy model mouse. Specific distribution of different lipid classes (fatty acids, triglycerides, phospholipids, tocopherol, coenzyme Q9, and cholesterol) allows us to distinguish three different regions on a mouse leg section: one is destroyed, another is degenerating (oxidative stress and deregulation of the phosphoinositol cycle), and the last one is stable. **TOF-SIMS imaging shows the ability to localize directly on a tissue section a great number of lipid compounds that reflect the state of the cellular metabolism.**—Touboul, D., A. Brunelle, F. Halgand, S. De La Porte, and O. Laprèvote. **Lipid imaging by gold cluster time-of-flight secondary ion mass spectrometry: application to Duchenne muscular dystrophy.** *J. Lipid Res.* 2005. 46: 1388–1395.

**Supplementary key words** colocalization • oxidative stress • degeneration • destructured cells

In lipidomics, as in all biological domains, the simultaneous localization of numerous organic compounds in tissue sections is a crucial issue for understanding cellular metabolic processes. New tools are developed to acquire the maximum amount of data in a short time, and the use of mass spectrometry images to manage information on biological tissue surfaces is increasing rapidly.

Two mass spectrometry imaging methods have been developed. The first one is based on matrix-assisted laser de-

sorption ionization (MALDI) (1, 2) coupled with a time-of-flight (TOF) technique, which leads to the acquisition of images in a mass range from 500 to a few tens of thousands daltons with a spatial resolution of  $\sim 50 \mu\text{m}$  (3, 4), and the second one is based on TOF secondary ion mass spectrometry (SIMS), which leads to the acquisition of images with masses of  $< 1,000 \text{ Da}$  with a spatial resolution of  $1 \mu\text{m}$  or less (5–7). In both cases, tissue sections having a thickness of 10–20  $\mu\text{m}$  are cut using a cryostat at  $-20^\circ\text{C}$  and transferred to target plates (stainless steel or glass). For MALDI-TOF experiments, the matrix is deposited by air spray, whereas no preliminary sample coating is needed for TOF-SIMS experiments. A laser (MALDI) or a focused ion beam (SIMS), both pulsed, irradiates the sample at each surface element, which is called a spot, and from which a mass spectrum is acquired and recorded. Each spot corresponds to a pixel of the image, and the intervals between each spot define the lateral resolution. The inevitable use of a matrix could be a weakness of the MALDI technique: homogeneous deposition by air spray is difficult to control, and the signal visibility is low for  $m/z < 600$  because of mass interference with matrix ion peaks (8). Tandem mass spectrometry imaging experiments can extend the accessible mass range down to  $m/z \sim 100\text{--}200$ , but to the detriment of the spatial resolution, which is only  $500 \mu\text{m}$  with present tandem mass spectrometers (9). Future improvements are expected toward a better spatial resolution of 1–10  $\mu\text{m}$  in association with reasonable data acquisition time (10, 11).

For three decades, TOF-SIMS has been used to localize molecular ions as well as elemental ions. With the former ion sources, such as  $\text{Ga}^+$  and  $\text{In}^+$  liquid metal ion guns, the images obtained from tissue sections were limited in

Manuscript received 16 February 2005 and in revised form 5 April 2005.

Published, JLR Papers in Press, April 16, 2005.  
DOI 10.1194/jlr.M500058.JLR200

<sup>1</sup> To whom correspondence should be addressed.  
e-mail: alain.brunelle@icsn.cnrs-gif.fr

Copyright © 2005 by the American Society for Biochemistry and Molecular Biology, Inc.

This article is available online at <http://www.jlr.org>

mass to ions such as the phosphocholine head group ( $m/z$  184) (12). The ability of TOF-SIMS coupled with a gold cluster ion source (13) to acquire molecular ion images of biological samples at a micrometer scale was demonstrated recently (14, 15). The useful lateral resolution is  $\sim 400$  nm with a mass range extended to  $m/z$  1,000. This technique needs neither water/ethanol washing nor matrix deposition. These advantages allow one to preserve the integrity of the biological material and to avoid the possible delocalization of cell markers. Moreover, this technique provides a high rate of fragmentation, which can be used for the identification of ions by structural analysis. To our knowledge, only brain sections (14, 15) and single cells (16) have been analyzed by TOF-SIMS and cluster TOF-SIMS imaging, and no study linked to a molecular disease has been developed with this method.

A recent study by MALDI-TOF imaging mass spectrometry showed a modification of the phosphatidylcholine composition between two areas of a mouse leg muscle section. The mouse was a model of Duchenne muscular dystrophy (DMD). This variation was linked to a cellular fusion process and indicated a regeneration in a destructured area of the muscle (17).

DMD is a neuromuscular inherited, autosomal recessive disease affecting  $\sim 1$  in 3,500 boys. This pathology is characterized by mutations on the X chromosome leading to a lack of dystrophin. Dystrophin is a 427 kDa cytoskeletal protein linked to the sarcoglycan-sarcospan and dystroglycan complexes and to actin, syntrophin, and dystrobrevin. The lack of dystrophin is involved in a complete destruction of the submembrane complexes. Clinical symptoms are muscular fibrosis, inflammatory reactions, and vascular dysfunction. For DMD patients, necrotic muscles are replaced by fibrous connective and adipose tissues. Blake and coworkers provide a recent review (18).

The *mdx* mouse model of DMD has been genetically selected for a point mutation on exon 23 of the DMD gene (19). Unlike DMD patients, few infiltrations by connective or adipose tissues have been observed for these dystrophin-deficient animals, and their longevity is not decreased significantly. However, they are good models in which to study the muscle regeneration-degeneration mechanism (20).

Modifications of the lipid composition of dystrophin-deficient muscle investigated by radiolabeling, gas, or thin-layer chromatography (21, 22) and oxidative damage (23–25) have been demonstrated for DMD patients and model mice. Nevertheless, the most important difficulty remains the fact that in muscle biopsies the muscle fibers are mixed with adipose and conjunctive tissues and can hardly be separated. That is why we decided to study the lipid composition of different areas of a *mdx* mouse leg section by gold cluster TOF-SIMS imaging.

## MATERIALS AND METHODS

### Sample preparation

*mdx* mouse (male, 3 weeks old) legs were frozen in isopentane and cooled to  $-160^\circ\text{C}$  in liquid nitrogen. They were cut at a temper-

ature of  $-20^\circ\text{C}$  using a cryostat (model MGW Lauda 1720; Leica Microsystems SA, Rueil-Malmaison, France) at a thickness of 20  $\mu\text{m}$ . The tissue sections were deposited onto a stainless-steel plate and stored at  $-80^\circ\text{C}$ . After drying under a pressure of a few hectopascals for 15 min, they were analyzed directly in the mass spectrometer.

### Image acquisition

A TOF-SIMS IV mass spectrometer (Ion-Tof GmbH, Münster, Germany) fitted with a gold cluster ( $\text{Au}_3^+$ ) ion source was used for these experiments. The primary ions impinge the surface of the tissue section with a kinetic energy of 25 keV and an incidence angle of  $45^\circ$ . The primary ion current, measured with a Faraday cup on the sample holder, is  $\sim 0.05$  pA for  $\text{Au}_3^+$  at 10 kHz. The primary ion dose is between  $4.7 \times 10^{11}$  ions/ $\text{cm}^2$  and  $10^{12}$  ions/ $\text{cm}^2$ . The secondary ions are extracted with an energy of 2 keV and are postaccelerated to 10 keV just before hitting the detector surface (single channel plate followed by a scintillator and a photomultiplier). A low-energy electron flood gun is activated to neutralize the surface during the analysis. The effective ion flight path is  $\sim 2$  m using a reflectron, and the mass resolution is  $\sim 6,300$  full width at half maximum (FWHM) at  $m/z$  35 and 10,000 (FWHM) at  $m/z$  795.7. The field of view is  $500 \times 500$   $\mu\text{m}^2$  ( $256 \times 256$  pixels). To increase the contrast, the images can be compressed to  $128 \times 128$  pixels (final resolution, 3.9  $\mu\text{m}$ ) during the data processing and an averaging process can be applied. The name of the compounds or the  $m/z$  value of the peak centroid, the maximal number of counts in a pixel (mc), and the total number of counts are shown below each image. The color scales correspond to the interval [0, mc].

### Mass calibration and ion peak identification

Because of the very low initial kinetic energy distribution of the secondary ions (26), the relationship between the time of flight and the square root of  $m/z$  is always linear. Consequently, the internal mass calibration can be made initially with  $\text{H}^+$ ,  $\text{H}_2^+$ , and  $\text{CH}_3^+$  ions in the positive ion mode and with  $\text{H}^-$ ,  $\text{C}^-$ ,  $\text{CH}^-$ ,  $\text{CH}_2^-$ ,  $\text{C}_2^-$ , and  $\text{C}_2\text{H}^-$  ions in the negative ion mode. To further improve the mass accuracy, the mass calibration was refined according to the following procedure. As an example, in the negative ion mode,  $m/z$  79 and 97 ions are identified as  $\text{PO}_3^-$  and  $\text{H}_2\text{PO}_4^-$  ions, respectively, with a precision of 2 ppm. The mass calibration is then refined by adding these two ions, enabling the identification of ions with  $m/z$  values between 251 and 283. Some of these ions are again added to the mass list used for the mass calibration, making it possible to improve the accuracy of the mass measurement above  $m/z$  300. Then, the mass assignments are made according to the following observations. First, the investigated ions have an odd  $m/z$  value, which means that the corresponding compounds contain an even number of nitrogen atoms (0, 2, 4, ...). Second, the difference between two consecutive monoisotopic peaks is always 2 Da in the groups of peaks located between  $m/z$  643 to 749 and  $m/z$  829 to 882, and an increment of 28 Da separates each of these groups of peaks. This suggests the presence of compounds containing one or several of the fatty acids already identified above. Finally, only lipids, which are the major constituents of cells, have been observed in tissue section TOF-SIMS imaging. Thus, it is possible to conclude that the group of ion peaks at  $m/z$  643–749 corresponds to phosphatidic acids (PAs), whereas the group of ion peaks at  $m/z$  829–882 is attributed to triglycerides (TGs).

## RESULTS

All compounds were identified according to the procedure described in Materials and Methods (Table 1). The

TABLE 1. Main ions recorded in the positive and negative ion modes, with the measured  $m/z$  values, the  $m/z$  values of the proposed ion structures, and the deviation in ppm

Ion Mode	Ion Species	Measured $m/z$	Calculated $m/z$	Ion $m/z$ Error ppm
Positive	Trimethylammonium	60.0812	60.0808	7.1
	Choline fragment	86.0960	86.0964	-4.8
	Choline	104.1062	104.1070	-7.3
	Phosphocholine	184.0747	184.0733	7.4
	Vitamin E	430.3757	430.3805	-11.3
	Phospholipids	734.5682	734.5645	5.0
Negative	Phosphoinositol fragment	760.5885	760.5851	4.5
	Phosphoinositol fragment	223.0051	223.0013	17.0
	Phosphoinositol fragment	241.0147	241.0119	11.7
	C16:2	251.2052	251.2017	14.2
	C16:1	253.2195	253.2173	8.7
	C16:0	255.2314	255.2330	-6.2
	C18:3	277.2198	277.2173	9.0
	C18:2	279.2313	279.2329	-5.9
	C18:1	281.2486	281.2486	-0.1
	C18:0	283.2609	283.2643	-12
	C20:4	303.2353	303.2329	7.8
	Cholesterol	385.3467	385.3476	2.3
	Vitamin E	429.3705	429.3738	-7.7
	Coenzyme Q9	795.6320	795.6297	2.9
	Phosphatidic acids	675.5013	675.4970	6.3
		701.5270	701.5127	20.4
	Triglycerides		829.7789	829.7291
		857.8163	857.7603	65.2

spectra acquired in the positive and negative modes are shown in **Fig. 1A, B**, respectively. **Figures 2, 3** show ion density maps recorded in the positive and negative ion modes, respectively. The areas where the images were recorded are very close to each other, as can be seen with the help of the position marks in both optical images (Figs. 2A, 3A). Furthermore, the two images were recorded at the edge of an area defined below as an “unstructured area.” This area has been described as an area undergoing regeneration (17).

### Phosphatidylcholine compounds

In the positive ion mode, the main class of observed phospholipids corresponds to phosphocholine compounds (PCs; Fig. 2H). Besides the molecular ion peaks ( $m/z$  730–810), some characteristic fragments are detected: trimethylammonium ion ( $m/z$  60; Fig. 2C), choline fragment ( $m/z$  86; Fig. 2D), choline head group ( $m/z$  104; Fig. 2E), and the phosphocholine head group ( $m/z$  184; Fig. 2F). All of these ions have a quaternary ammonium function that induces a very high secondary ion emission yield compared with the other families of phospholipids. It should be noted that the PC ion emission yield is lowest in the intercellular spaces, which are extremely poor in PC. This observation shows that our sample preparation is not accompanied by any molecular delocalization beyond  $\sim 1 \mu\text{m}$ .

From the images of PC and fragment ions, the structured and unstructured areas are easily observed. These images are perfectly correlated with the optic image (Fig. 2A) and the total ion image (Fig. 2B) and offer a quick overview of the tissue structure. Unfortunately, the contrast of the PC image is too low to provide some spatial in-

formation (Fig. 2H). Nonetheless, a slight accumulation of PC fragments is observed in the structured area, but it seems not to be significant (Fig. 2D–F).

The phospholipid composition of samples from patients with DMD (21, 22) or from *mdx* mice has already been studied (27, 28). In most cases, no significant modification of PC abundance has been described. Therefore, the TOF-SIMS images do not disagree with the previous data.

The images show perfectly the cell bodies that correspond to muscular fibers that were cut transversally. Dark areas inside the cells correspond to the nuclei. It can be observed that the high level of central nucleation of this muscular tissue is characteristic of regenerated muscle (29).

### Antioxidant compounds

Tocopherol (vitamin E) ion peaks are clearly observed in both positive (Fig. 2G) and negative (Fig. 3N) ion modes. The image in the positive ion mode shows a lower contrast than that in the negative ion mode and does not show any accumulation in any area. Nevertheless, in the negative ion mode, the tocopherol ion intensity is higher in the central area, between the destructured area to the left and an apparently healthy region to the right. In the negative ion mode, the ion intensity of coenzyme Q9, which is the predominant form of coenzyme Q for rats and mice, is higher in the region where the vitamin E signal is concentrated (Fig. 3O). In the same zone, two subareas can be defined: the first is located in the top part, where the ion intensities are very high (surrounded by a red line), and the second is located in the bottom part, where the ion intensities are more diffuse (surrounded by a green line).

### PAs and phosphoinositol fragments

In the negative ion mode, ion peaks of PAs are clearly observed (Fig. 3P). Ions at  $m/z$  223.2 and 241.2 (Fig. 3C, D, respectively) correspond to specific fragments of phosphatidylinositols (PIs): phosphatidylinositol phosphate (PIP) and phosphatidylinositol biphosphate (PIP<sub>2</sub>) (30). The molecular ions of the PI and its derivatives are not observed because of low concentrations or high fragmentation rates.

The PAs are concentrated in the areas surrounded in red and green. The PI fragment ions are abundant in the area surrounded in green. Only a residual and diffuse signal is observed in the red zone.

Accumulations of PAs and PIs in the regions surrounded in red and green, just at the edge of the destructured area, can be linked to an important disorder of lipid metabolism, which is related to high free calcium levels in *mdx* mouse muscle (31).

### Fatty acids, diglycerides, and TGs

A significant accumulation of TGs is seen in the region surrounded in green (Fig. 3Q). This can correspond to adipose tissues or to a lipid metabolism disorder at the edge of the structured area.

The FA carboxylate ions are also accumulated in the region surrounded in green (Fig. 3E–L). These ions can be



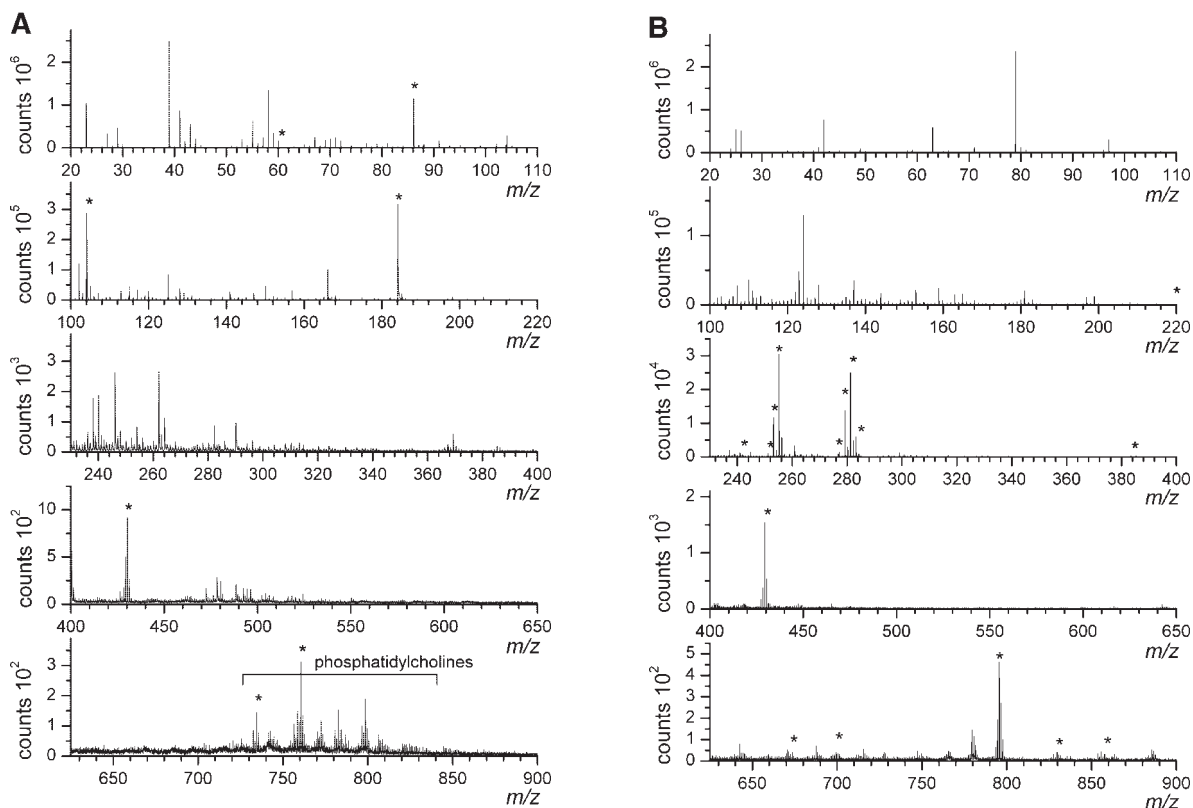


**Fig. 1.** A: Positive ion time-of-flight secondary ion mass spectrometry (TOF-SIMS) mass spectrum. Area of  $500 \times 500 \mu\text{m}^2$  on a *mdx* mouse leg section. *m/z* values and identification of areas labeled with stars are reported in Table 1. B: Same as A in the negative ion mode.

either free fatty acids or specific fragments of TG or phospholipids. The colocalization of the FA and TG ions on the tissue section led us to think that the FA ions could arise from the fragmentation of the TG during the primary ion bombardment. Indeed, tandem mass spectrometry experiments have shown that the deprotonated molecules ( $[\text{M-H}]^-$ ) generated by electrospray from TGs dissociate into fatty acid carboxylate anions (32).

The relative intensities of different FA ions can be calculated directly because the secondary ion emission yields of these compounds are almost equal as a result of their closely related physicochemical properties. The study of the composition in C16:n and C18:n, which are the predominant FA structures, led us to distinguish three different areas in Figs. 3, 4. The first region is the destructured area, where the intensity ratio between C18:0 and C18:1 ions is equal to  $0.91 \pm 10^{-4}$ . The second region corresponds to the intermediate region, where this ratio is equal to  $0.118 \pm 0.004$ . The third region is the blue region, where the ratio is close to  $0.165 \pm 0.01$  (Fig. 4C). In the same way, we observed a slight change in the intensity ratio between C16:0 and C16:1 (Fig. 4B). The other relative FA ratios are not significant (data not shown).

An accumulation of arachidonic acid (C20:4 at *m/z* 303.18; Fig. 3L) is observed in the green area.

### Cholesterol

Cholesterol ion peaks are observed in both negative and positive ion modes, but in the positive mode, the in-

tensity is too low to provide images with sufficient contrast (data not shown). In the negative ion mode, cholesterol (Fig. 3M) is concentrated in the intermediate and destructured area.

## DISCUSSION

### Area under inflammatory reaction and degeneration

The colocalization of vitamin E and the reduced form of coenzyme Q9, which are antioxidant compounds, reveals a high level of oxidative stress in the regions surrounded in green and red in Fig. 3. Many studies have reported indications of oxidative damage, such as higher contents of oxidized proteins, antioxidant protein gene expression, lower contents of free protein thiol groups, and peroxidation of lipids for dystrophin-deficient muscle compared with control muscle (22–24). Moreover, a review by Murphy and Kehrer (23) mentioned an increase in antioxidant molecule concentration, specifically vitamin E, in dystrophin-deficient muscles. Nevertheless, all of these studies are based on biopsies and reflect only the global state of the organ. No measurement at the cellular level of this kind of biomarker has been reported.

One of the origins of oxidative stress is the increase of the nitric oxide ( $\text{NO}^\cdot$ ) level that is provided by nitric oxide synthase (NOS).  $\text{NO}^\cdot$  has both a destructive and a protective role. It can react with the superoxide  $\text{O}_2^{\cdot-}$  to form peroxynitrite, a highly oxidant molecule, and it can also

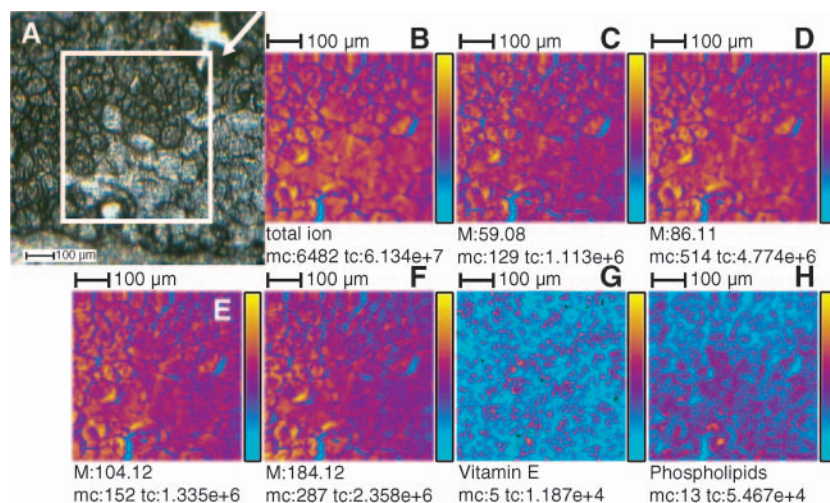


**Fig. 2.** A: Optical image of a *mdx* mouse leg section. The area in the white square corresponds to the area analyzed in the positive ion mode ( $500 \times 500 \mu\text{m}^2$ ). The white arrow indicates the position mark. B to H: Images corresponding to the following ions: total ion image (sum of all ion intensities; B);  $m/z$  60 (trimethylammonium; C);  $m/z$  86 (fragment of choline; D);  $m/z$  104 (choline; E);  $m/z$  184 (phosphocholine; F);  $m/z$  427–432 (ions of vitamin E; G); and  $m/z$  700–850 (glycerophosphatidylcholine ions; H). mc, maximal number of counts in a pixel; tc, total number of counts.

recombine with free radicals generated by inflammatory cells (33, 34). In the case of DMD, the lack of dystrophin induces a destabilization of the cell membrane, in particular, NOS migration to the cytosol (35). The importance of

NOS has been demonstrated by Wehling, Spencer, and Tidball (36). Indeed, a NOS transgene reduces the effects of muscular dystrophy for *mdx* mice. Particularly, muscle membrane injuries decrease as well as serum creatine ki-

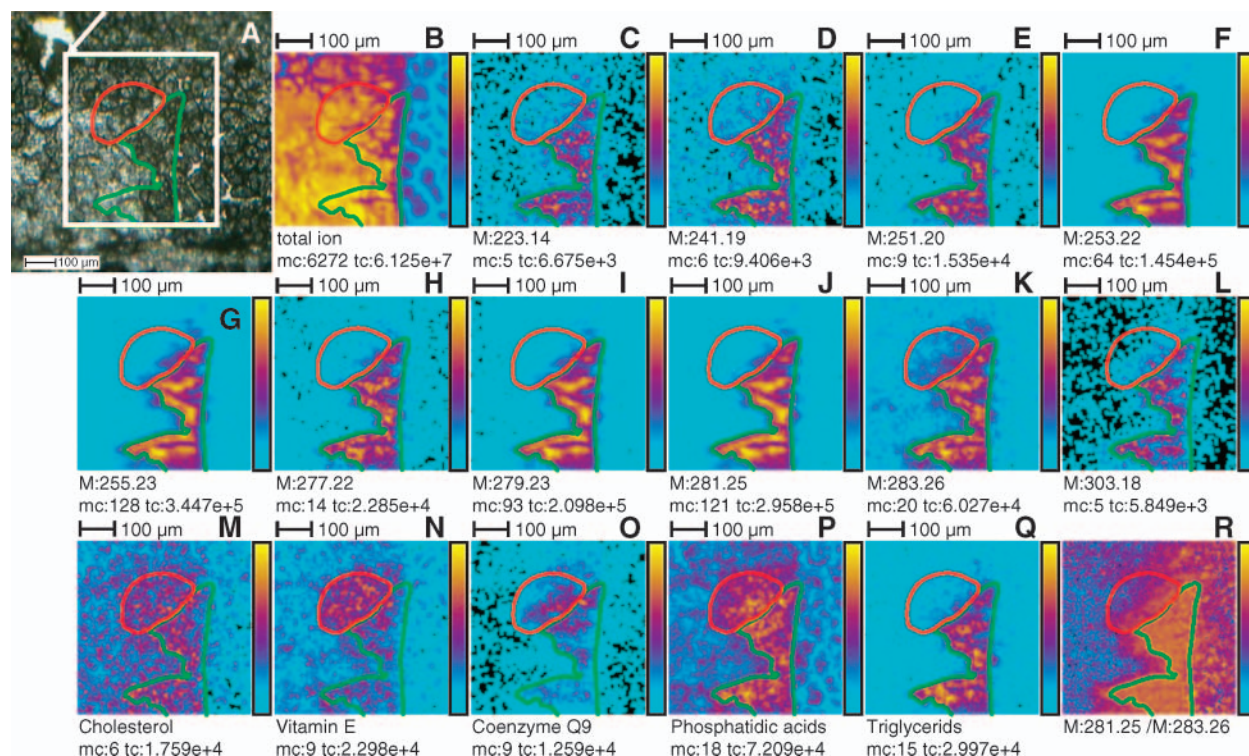


**Fig. 3.** A: Optical image of a *mdx* mouse leg section. The area in the white square corresponds to the area analyzed in the negative ion mode ( $500 \times 500 \mu\text{m}^2$ ). The white arrow indicates the position mark. B to Q: Images corresponding to the following ions: total ion image (sum of all ion intensities; B);  $m/z$  223 (fragment of phosphatidylinositol; C);  $m/z$  241 (fragment of phosphatidylinositol; D);  $m/z$  251 (C16:2 fatty acid; E);  $m/z$  253 (C16:1 fatty acid; F);  $m/z$  255 (C16:0 fatty acid; G);  $m/z$  277 (C18:3 fatty acid; H);  $m/z$  279 (C18:2 fatty acid; I);  $m/z$  281 (C18:1 fatty acid; J);  $m/z$  283 (C18:0 fatty acid; K);  $m/z$  303 (C20:4 fatty acid; L);  $m/z$  383–387 (cholesterol; M);  $m/z$  427–432 (vitamin E; N);  $m/z$  795–797 (coenzyme Q9; O);  $m/z$  643–749 (phosphatidic acids; P); and  $m/z$  829–882 (triglycerides; Q). R: Intensity ratio between the ions at  $m/z$  281 and  $m/z$  283. The red and green lines indicate the different regions described in the text. mc, maximal number of counts in a pixel; tc, total number of counts.

nase concentration, which is a marker of DMD. It is assumed that NO<sup>•</sup> protects muscles against oxidative injury and that this protection is reduced in dystrophic muscle. Our results tend to confirm this hypothesis. The accumulations of vitamin E and coenzyme Q9 are significant markers of oxidative stress and inflammatory reactions, which can induce muscle necrosis.

The colocalization of vitamin E, coenzyme Q9, and PA supports the hypothesis that high oxidative stress and inflammatory reactions could occur at the edge of the destructured area. The area surrounded in green, and in some degree the red area, can be considered a degenerative area.

Cholesterol is a molecule incorporated in the membrane that allows its fluidity to modulate. A greater amount

of cholesterol corresponds to a decrease of membrane fluidity. This process is known to be related to the degeneration-regeneration process of muscular fibers (37).

### Disorders of the phosphoinositide cycle

The digestion of phospholipids, particularly PC, by phospholipase D (PLD) is a source of PA. It has been clearly established that the level of free calcium is strongly modified in dystrophin-deficient muscles (31, 38). Now the PLD is known to be activated in the presence of calcium (39, 40). Therefore, a high concentration of free calcium can induce an increase of PLD activity and consequently an accumulation of PA in some areas of dystrophin-deficient muscle.

Another origin of PA is the catalytic cycle of the phosphoinositides. PI, PIP, and PIP<sub>2</sub> are metabolized by the phospholipase C to give diglyceride/diacylglycerol. Diglyceride/diacylglycerol is then converted into PAs, FAs, or TGs. PAs are finally transformed into cytidine diphosphate diglycerides, which react with the inositol to be converted into PIs. The accumulation of fragments of PI derivatives in the same area as the PAs, FAs, and TGs could be explained as disorders in the phosphoinositide cycle. Moreover, it has been demonstrated that the level of inositol 1,4,5-triphosphate is two times higher in dystrophin-deficient cells or muscles compared with control ones (41). Some results tend to show that the PI turnover is decreased slightly in dystrophin-deficient cells and can lead to an accumulation of PA (42). Finally, Brown et al. (43) have demonstrated that PIP<sub>2</sub> can also stimulate the activity of PLD and lead to an accumulation of PA. Thus, all of these facts indicate that the area surrounded in green undergoes a strongly disturbed phosphoinositide cycle.

The accumulation of FA can be linked to the fragmentation of TG and to disorders of the phosphoinositide cycle. Moreover, a study by Lindahl et al. (44) described an increase of phospholipase A<sub>2</sub> activity in dystrophin-deficient muscles of patients with DMD. This enzyme is responsible for the degradation of the phospholipids in FA and lysophospholipids. Its activity, which increases in the presence of Ca<sup>2+</sup> or oxidative stress (45, 46), can be linked to the formation of numerous inflammatory mediators such as prostaglandins (47, 48) via arachidonic acid C20:4 and also can be linked to the chronic inflammation observed in dystrophin-deficient muscles (49). This FA is the precursor of numerous leukotrienes and prostaglandins, which are proinflammatory molecules.

The fatty acid composition of the different areas of the tissue section clearly shows an increase of the intensity ratio between C18:0 and C18:1 and between C16:0 and C16:1 in the red zone of Fig. 4A. This change could be explained by the trend of the dystrophin-deficient cells in the destructured area to compensate for the partial destruction of their membrane by incorporating saturated FA to increase their stability.

### Area under regeneration

The destructured area does not show any significant accumulation of compounds. The regenerative character of

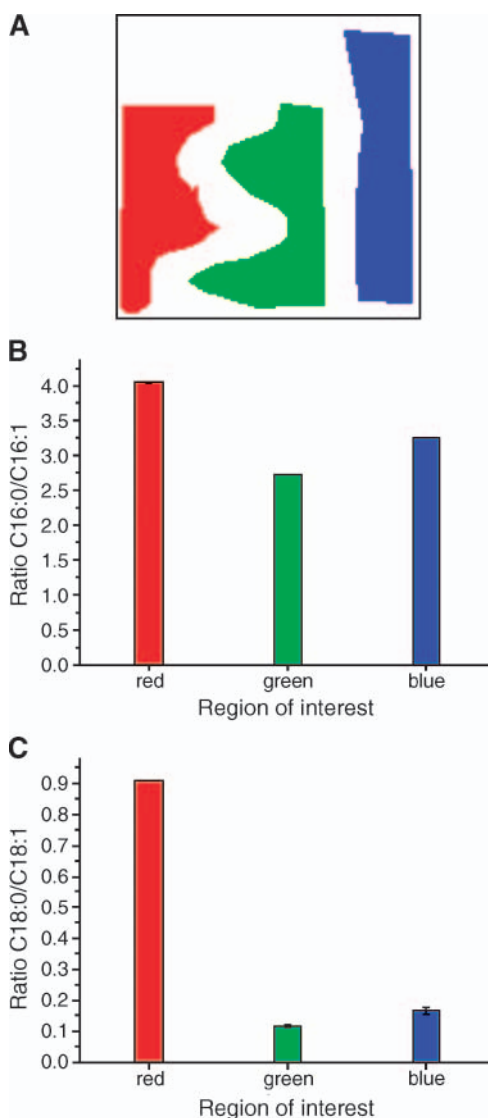




**Fig. 4.** A: Regions of interest from which spectra are extracted. The destructured area is red, the intermediate area under regeneration is green, and the stable area is blue. The three colors have the same identification in B and C. B: C16:0-to-C16:1 ion peak intensity ratio. C: C18:0-to-C18:1 ion peak intensity ratio. Nonvisible error bars are not greater than the borderline thickness. Error bars indicate SEM.



this area has been determined previously by MALDI-TOF imaging experiments (17). A change in the PC composition was described and linked to the phenomenon of cell fusion. We have suggested a role of the NOS in the degenerative processes at the edge of the regenerative area. It should be observed that NO<sup>•</sup> could also activate the muscle satellite cells and induce the regeneration of the tissue (50).

### Conclusion

TOF-SIMS imaging coupled to a gold cluster ion source has shown its ability to simultaneously determine the localization of various lipid compounds on a tissue without any specific preparation. Four different regions of a *mdx* mouse leg section can be distinguished: one undergoing oxidative stress, a second one degenerating, a third one regenerating, and the last one stable. No treatment was necessary to acquire these images, allowing the integrity of the biological samples to be preserved. Currently, no other imaging technique can generate such a great amount of data with a single data acquisition at the micrometer scale. TOF-SIMS imaging is revealed as a great tool for lipid analysis at the cellular level on a tissue section. This technique would benefit from the development of tandem mass spectrometry-like methods, which would lead to a refined structure determination of diagnostic ions. New primary cluster ion sources and optimized sample preparation methods are also expected to further extend the useful mass range and to favor the desorption of labile compounds.  

Ion-Tof GmbH (Münster, Germany) and TASCION GmbH (Münster, Germany) are warmly thanked for their material support. D.T. is indebted to the Institut de Chimie des Substances Naturelles (Centre National de la Recherche Scientifique) for a Ph.D. research fellowship.

### REFERENCES

- Karas, M., D. Bachmann, U. Bahr, and F. Hillenkamp. 1987. Matrix-assisted ultraviolet laser desorption of non-volatile compounds. *Int. J. Mass Spectrom. Ion Process.* **78**: 53–68.
- Hillenkamp, F., and M. Karas. 2000. Matrix-assisted laser desorption/ionisation, an experience. *Int. J. Mass Spectrom.* **200**: 71–77.
- Stoeckli, M., P. Chaurand, D. E. Hallahan, and R. M. Caprioli. 2001. Imaging mass spectrometry: a new technology for the analysis of protein expression in mammalian tissues. *Nat. Med.* **7**: 493–496.
- Chaurand, P., S. A. Schwartz, and R. M. Caprioli. 2004. Profiling and imaging proteins in tissue sections by MS. *Anal. Chem.* **76**: 87A–93A.
- Castaing, R., and G. Slodzian. 1962. Microanalyse par emission ionique secondaire. *J. Microsc.* **1**: 395–410.
- Benninghoven, A., and E. Loebach. 1971. Tandem mass spectrometer for secondary ion studies. *Rev. Sci. Instrum.* **42**: 49–52.
- Belu, A. M., D. J. Graham, and D. G. Castner. 2003. Time-of-flight secondary ion mass spectrometry: techniques and applications for the characterization of biomaterial surfaces. *Biomaterials.* **24**: 3635–3653.
- Schwartz, S. A., M. L. Reyzer, and R. M. Caprioli. 2003. Direct tissue analysis using matrix-assisted laser desorption/ionization mass spectrometry: practical aspects of sample preparation. *J. Mass Spectrom.* **38**: 699–708.
- Reyzer, M. L., Y. Hsieh, K. Ng, W. A. Korfmacher, and R. M. Caprioli. 2003. Direct analysis of drug candidates in tissue by matrix-assisted laser desorption/ionization mass spectrometry. *J. Mass Spectrom.* **10**: 1081–1092.
- Spengler, B., and M. Hubert. 2002. Scanning microprobe matrix-assisted laser desorption ionization (SMALDI) mass spectrometry: instrumentation for sub-micrometer resolved LDI and MALDI surface analysis. *J. Am. Soc. Mass Spectrom.* **13**: 735–748.
- Piyadasa, G., J. R. McNabb, V. Spicer, G. S. Standing, and W. Ens. 2004. Imaging MALDI with an orthogonal TOF mass spectrometer. Proceedings of the 52nd American Society for Mass Spectrometry. Conference on Mass Spectrometry and Allied Topics, Nashville, Tennessee, May 23–27, 2004.
- Todd, P. J., T. G. Schaaff, P. Chaurand, and R. M. Caprioli. 2001. Organic ion imaging of biological tissue with secondary ion mass spectrometry and matrix-assisted laser desorption/ionization. *J. Mass Spectrom.* **36**: 355–369.
- Benguerba, M., A. Brunelle, S. Della-Negra, J. Depauw, H. Joret, Y. Le Beyec, M. G. Blain, E. A. Schweikert, G. Ben Assayag, and P. Sudraud. 1991. Impact of slow gold clusters on various solids. Non linear effects in secondary ion emission. *Nucl. Instrum. Methods Phys. Res. B.* **62**: 8–22.
- Touboul, D., F. Halgand, A. Brunelle, R. Kersting, E. Tallarek, B. Hagenhoff, and O. Laprevote. 2004. Tissue molecular ion imaging by gold cluster ion bombardment. *Anal. Chem.* **76**: 1550–1559.
- Sjövall, P., J. Jausmaa, and B. Johansson. 2004. Mass spectrometric imaging of lipids in brain tissue. *Anal. Chem.* **76**: 4271–4278.
- Sjövall, P., J. Lausmaa, H. Nygren, L. Carlsson, and P. Malmberg. 2003. Imaging of membrane lipids in single cells by imprint-imaging time-of-flight secondary ion mass spectrometry. *Anal. Chem.* **75**: 3097–3102.
- Touboul, D., H. Piednoël, V. Voisin, S. De La Porte, A. Brunelle, F. Halgand, and O. Laprevote. 2004. Characterisation of a lipid marker of Duchenne muscular dystrophy by MALDI-TOF-mass spectrometry and mass spectrometry-imaging. *Eur. J. Mass Spectrom.* **10**: 657–664.
- Blake, D. J., A. Weir, S. E. Newey, and K. E. Davies. 2002. Function and genetics of dystrophin and dystrophin-related proteins in muscle. *Physiol. Rev.* **82**: 291–329.
- Bulfield, G., W. G. Siller, P. A. Wight, and K. J. Moore. 1984. X chromosome-linked muscular dystrophy (*mdx*) in the mouse. *Proc. Natl. Acad. Sci. USA.* **81**: 1189–1192.
- De La Porte, S., S. Morin, and J. Koenig. 1999. Characteristics of skeletal muscle in *mdx* mutant mice. *Int. Rev. Cytol.* **191**: 99–148.
- Ionasescu, V., L. Monaco, A. Sandre, R. Ionasescu, L. Burmeister, C. Depresse, and L. Z. Stern. 1981. Alterations in lipid incorporation in Duchenne muscular dystrophy. *J. Neurol. Sci.* **50**: 249–257.
- Kunze, D., E. Reichmann, E. Egger, D. Olthoff, and K. Döhler. 1975. Fatty acid pattern of lipids in normal and dystrophic human muscle. *Eur. J. Clin. Invest.* **5**: 471–475.
- Murphy, M. E., and J. P. Kehr. 1989. Oxidative stress and muscular dystrophy. *Chem. Biol. Interact.* **69**: 101–173.
- Disatnik, M. H., J. Dhawan, Y. Yu, M. Flint Beal, M. M. Whirl, A. A. Franco, and T. A. Rando. 1998. Evidence of oxidative stress in *mdx* mouse muscle: studies of the pre-necrotic state. *J. Neurol. Sci.* **161**: 77–84.
- Rando, T. A., M. H. Disatnik, Y. Yu, and A. Franco. 1998. Muscle cells from *mdx* mice have an increased susceptibility to oxidative stress. *Neuromuscul. Disord.* **8**: 14–21.
- Veryovkin, I. V., S. F. Belykh, A. Adriaens, A. V. Zinovev, and F. Adams. 2004. On the trends in kinetic energies of secondary ions produced by polyatomic ion bombardment. *Appl. Surf. Sci.* **231–232**: 101–105.
- Owens, K., and B. P. Hughes. 1970. Lipids of dystrophic and normal mouse muscle: whole tissue and particulate fractions. *J. Lipid Res.* **11**: 486–495.
- Anderson, J. E. 1991. Myotube phospholipid synthesis and sarcolemma ATPase activity in dystrophic (*mdx*) mouse muscle. *Biochem. Cell Biol.* **69**: 835–841.
- DiMario, J. X., A. Uzman, and R. C. Strohman. 1991. Fiber regeneration is not persistent in dystrophic (MDX) mouse skeletal muscle. *Dev. Biol.* **148**: 314–321.
- Hsu, F. F., and J. Turk. 2000. Characterization of phosphatidylinositol, phosphatidylinositol-4-phosphate, and phosphatidylinositol-4,5-bisphosphate by electrospray ionization tandem mass spectrometry: a mechanistic study. *J. Am. Soc. Mass Spectrom.* **11**: 986–999.

31. Turner, P. R., T. Westwood, C. M. Regen, and R. A. Steinhardt. 1988. Increased protein degradation results from elevated free calcium levels found in muscle from mdx mice. *Nature*. **335**: 735–738.
32. Stroobant, V., R. Rozenberg, E. M. Bouabsa, E. Deffense, and E. De Hoffmann. 1995. Fragmentation of conjugate bases of esters derived from multifunctional alcohol including triacylglycerols. *J. Am. Soc. Mass Spectrom.* **6**: 498–506.
33. Miles, A. M., D. S. Bohle, P. A. Glassbrenner, B. Hansert, D. A. Wink, and M. B. Grisham. 1996. Modulation of superoxide-dependent oxidation and hydroxylation reactions by nitric oxide. *J. Biochem. (Tokyo)*. **271**: 40–47.
34. Darley-Usmar, V., H. Wiseman, and B. Halliwell. 1995. Nitric oxide and oxygen radicals: a question of balance. *FEBS Lett.* **369**: 131–135.
35. Brenman, J. E., D. S. Chao, H. Xia, K. Aldape, and D. S. Bredt. 1995. Nitric oxide synthase complexed with dystrophin and absent from skeletal muscle sarcolemma in Duchenne muscular dystrophy. *Cell*. **82**: 743–752.
36. Wehling, M., M. J. Spencer, and J. G. Tidball. 2001. A nitric oxide synthase transgene ameliorates muscular dystrophy in mdx mice. *J. Cell Biol.* **155**: 123–131.
37. Fischbeck, K. H., E. Bonilla, and D. L. Schotland. 1983. Freeze-fracture analysis of plasma membrane cholesterol in Duchenne muscle. *Ann. Neurol.* **13**: 532–535.
38. Gailly, P. 2002. New aspects of calcium signaling in skeletal muscle cells: implications in Duchenne muscular dystrophy. *Biochim. Biophys. Acta*. **1600**: 38–44.
39. Walter, M., M. Tepel, J. R. Nofer, M. Neusser, G. Assmann, and W. Zidek. 2000. Involvement of phospholipase D in store-operated calcium influx in vascular smooth muscle cells. *FEBS Lett.* **479**: 51–56.
40. McDermott, M., M. J. Wakelam, and A. J. Morris. 2004. Phospholipase D. *Biochem. Cell Biol.* **82**: 225–253.
41. Liberona, J. L., J. A. Powell, S. Shenoi, L. Petherbridge, R. Caviedes, and E. Jaimovich. 1998. Differences in both inositol 1,4,5-trisphosphate mass and inositol 1,4,5-trisphosphate receptors between normal and dystrophic skeletal muscle cell lines. *Muscle Nerve*. **21**: 902–909.
42. Rounds, P. S., A. B. Jepson, D. J. McAllister, and J. L. Howland. 1980. Stimulated turnover of phosphatidylinositol and phosphatidate in normal and Duchenne-dystrophic human skin fibroblasts. *Biochem. Biophys. Res. Commun.* **97**: 1384–1390.
43. Brown, H. A., S. Gutowski, R. A. Kahn, and P. C. Sternweis. 1995. Partial purification and characterization of Arf-sensitive phospholipase D from porcine brain. *J. Biol. Chem.* **270**: 14935–14943.
44. Lindahl, M., E. Backman, G. Henriksson, R. Gorospe, and E. P. Hoffman. 1995. Phospholipase A2 activity in dystrophinopathies. *Neuromuscul. Disord.* **5**: 193–199.
45. Sevanian, A., and E. Kim. 1985. Phospholipase A2 dependent release of fatty acids from peroxidized membranes. *J. Free Radic. Biol. Med.* **1**: 263–271.
46. Baker, M. S., and L. Austin. 1989. The pathological damage in Duchenne muscular dystrophy may be due to increased intracellular OXY-radical generation caused by the absence of dystrophin and subsequent alterations in Ca<sup>2+</sup> metabolism. *Med. Hypotheses*. **29**: 187–193.
47. Jackson, M. J., M. H. Brooke, K. Kaiser, and R. H. Edwards. 1991. Creatine kinase and prostaglandin E2 release from isolated Duchenne muscle. *Neurology*. **41**: 101–104.
48. McArdle, A., A. Foxley, R. H. Edwards, and M. J. Jackson. 1991. Prostaglandin metabolism in dystrophin-deficient MDX mouse muscle. *Biochem. Soc. Trans.* **19 (Suppl.)**: 177.
49. Porter, J. D., S. Khanna, H. J. Kaminski, J. S. Rao, A. P. Merriam, C. R. Richmonds, P. Leahy, J. Li, W. Guo, and F. H. Andrade. 2002. A chronic inflammatory response dominates the skeletal muscle molecular signature in dystrophin-deficient mdx mice. *Hum. Mol. Genet.* **11**: 263–272.
50. Anderson, J. E. 2000. A role for nitric oxide in muscle repair: nitric oxide-mediated activation of muscle satellite cells. *Mol. Biol. Cell*. **11**: 1859–1874.